

# Graphene photodetectors for high-speed optical communications

Thomas Mueller<sup>†</sup>, Fengnian Xia<sup>\*</sup> and Phaedon Avouris<sup>\*</sup>

**Although silicon has dominated solid-state electronics for more than four decades, a variety of other materials are used in photonic devices to expand the wavelength range of operation and improve performance. For example, gallium-nitride based materials enable light emission at blue and ultraviolet wavelengths<sup>1</sup>, and high index contrast silicon-on-insulator facilitates ultradense photonic devices<sup>2,3</sup>. Here, we report the first use of a photodetector based on graphene<sup>4,5</sup>, a two-dimensional carbon material, in a 10 Gbit s<sup>-1</sup> optical data link. In this interdigitated metal-graphene-metal photodetector, an asymmetric metallization scheme is adopted to break the mirror symmetry of the internal electric-field profile in conventional graphene field-effect transistor channels<sup>6-9</sup>, allowing for efficient photo-detection. A maximum external photoresponsivity of 6.1 mA W<sup>-1</sup> is achieved at a wavelength of 1.55  $\mu\text{m}$ . Owing to the unique band structure of graphene<sup>10,11</sup> and extensive developments in graphene electronics<sup>12,13</sup> and wafer-scale synthesis<sup>13</sup>, graphene-based integrated electronic-photonic circuits with an operational wavelength range spanning 300 nm to 6  $\mu\text{m}$  (and possibly beyond) can be expected in the future.**

Graphene, a single layer of carbon atoms assembled in a honeycomb lattice, is currently the subject of intense research for condensed matter physicists and electronic engineers due to its exceptional electronic properties. Graphene also holds great promise for novel photonic devices<sup>10,14-19</sup>. Recent photocurrent generation experiments in graphene show a strong photoresponse near metal/graphene interfaces, with an internal quantum efficiency of 15–30% despite its gapless nature<sup>6,7,9</sup>. Moreover, graphene photodetectors can potentially operate at speeds >500 GHz (ref. 19). However, the external responsivity (or efficiency) of previously demonstrated graphene photodetectors was relatively small. Here, we report a simple vertical-incidence metal-graphene-metal (MGM) photodetector with external responsivity of 6.1 mA W<sup>-1</sup> at an operating wavelength of 1.55  $\mu\text{m}$ , representing a 15-fold improvement compared with a previous demonstration<sup>19</sup>. Such graphene photodetectors have been deployed in a 10 Gbit s<sup>-1</sup> optical data link for the first time and error-free detection of the optical bit stream was demonstrated, revealing the great potential of graphene in numerous applications related to light detection<sup>20-23</sup>.

A schematic view of the MGM photodetector is shown in Fig. 1. The geometry of this MGM photodetector is similar to that of traditional metal-semiconductor-metal (MSM) detectors<sup>24</sup>. Our MGM photodetectors were fabricated on a highly resistive silicon wafer (1–10 k $\Omega$  cm) with a 300-nm-thick layer of thermal oxide. Flakes of single-, bi- and tri-layer graphenes were identified<sup>25,26</sup> and confirmed by Raman spectroscopy, and interdigitated electrodes with a spacing of 1  $\mu\text{m}$  and width of 250 nm were then fabricated. One set of fingers was made of palladium/gold (20/25 nm in thickness), and the other of titanium/gold (20/25 nm). The active layer of this specific device was bi-layer graphene, and

unless otherwise specified, all results reported here were obtained from this device. The active detector area was 6  $\times$  6  $\mu\text{m}$ . The detector was connected to contact pads, each with an area of 80  $\times$  80  $\mu\text{m}$ , separated by 40  $\mu\text{m}$ .

In the graphene field-effect-transistor (FET) photodetectors demonstrated previously<sup>19</sup>, the internal (built-in) electric fields, which are responsible for the separation of the photo-generated carriers, only exist in narrow regions ( $\sim$ 0.2  $\mu\text{m}$ ) adjacent to the electrode/graphene interfaces, where charge transfer between the metal and graphene leads to band bending<sup>6-8</sup>. The absence of a strong electric field in the bulk graphene sheet, where most of the electron-hole pairs are generated, leads to carrier recombination without any contribution to the external photocurrent. In this work, multiple, interdigitated metal fingers are used, leading to the creation of a greatly enlarged, high  $E$ -field, light-detection region. However, if both electrodes in Fig. 1 consist of the same metal, the built-in electric field profile in the channel between two neighbouring fingers is symmetric<sup>6-9</sup>, and the total photocurrent is zero. Here, we demonstrate that an asymmetric metallization scheme can be used to break the mirror symmetry of the built-in potential profile within the channel, allowing for the individual contributions to be summed to give the overall photocurrent.

Figure 2a shows photocurrent images taken with different gate biases ( $V_G$ , between  $-60$  and 60 V) applied to the silicon backgate

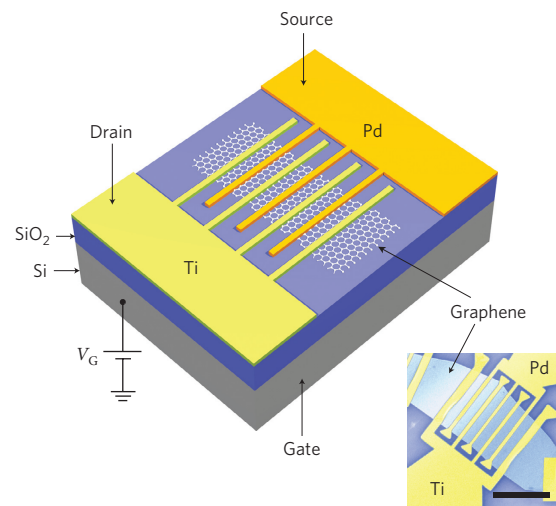


**Figure 1 | Metal-graphene-metal (MGM) photodetectors with asymmetric metal contacts.** Main panel: three-dimensional schematic of the MGM photodetector. Bottom right: scanning electron micrograph of the MGM photodetector. Scale bar, 5  $\mu\text{m}$ . The spacing between the metal fingers is 1  $\mu\text{m}$  and the finger width is 250 nm.

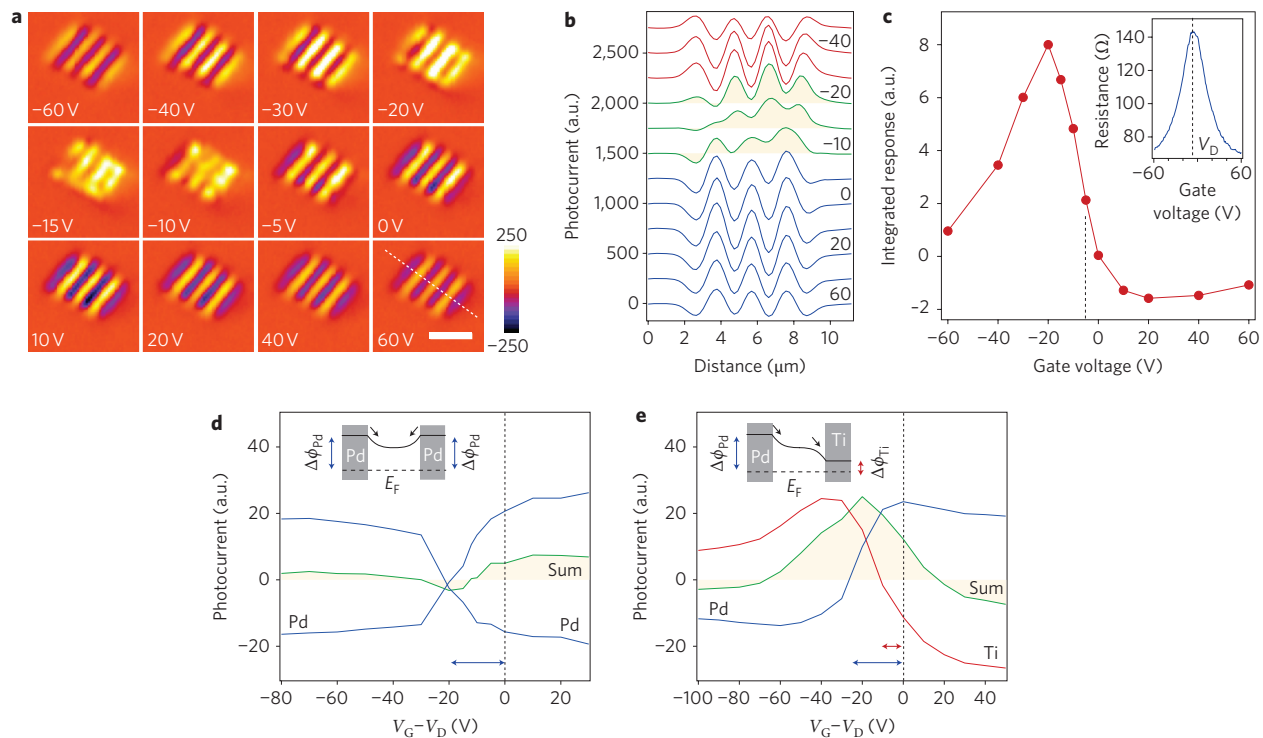


**Figure 2 | Photocurrent imaging in MGM photodetectors with excitation of 632.8 nm.** **a**, Photocurrent images of the MGM photodetectors taken at 12 gate biases from  $-60$  to  $60$  V. Scale bar,  $5\ \mu\text{m}$ . **b**, Photocurrent line scans of the same device at various gate biases from  $-60$  (top) to  $60$  V (bottom). The scan is performed along the white dashed line shown in the lower right corner of Fig. 2a. **c**, Integrated photocurrent response versus back-gate bias. Inset: graphene channel resistance versus back-gate bias. **d**, Blue lines: peak photocurrents around source and drain palladium contacts in a long-channel graphene device versus  $V_G - V_D$ , where  $V_G$  and  $V_D$  are the gate bias and Dirac point voltage, respectively. Green line: sum of both blue lines. Inset: band profile of this graphene FET. **e**, Blue (red) line: peak photocurrent around source palladium (drain titanium) in another long-channel graphene FET with asymmetric contacts versus  $V_G - V_D$ . Green line: sum of the blue and red lines. Inset: band profile of this graphene FET at  $V_G - V_D$  of  $-20$  V. Insets of **d** and **e**: the dotted line denotes the Fermi level.  $\Delta\phi_{\text{Pd}}$  and  $\Delta\phi_{\text{Ti}}$  represent the difference between the Dirac point energy and the Fermi level in palladium- and titanium-doped graphenes, respectively.

(see also the corresponding line scans in Fig. 2b). In these measurements, a focused laser beam (He-Ne laser; wavelength, 632.8 nm) is scanned over a device while the induced short-circuit photocurrent is measured as a function of laser spot position to obtain a spatial image with a resolution of  $\sim 0.6\ \mu\text{m}$  (ref. 7). (For further details see Methods.) At large negative voltages ( $V_G = -60$  and  $-40$  V), the images show stripes of alternating positive and negative polarity. The integrated response, shown in Fig. 2c, is close to zero, as expected, due to rather symmetric potential profile within the graphene channel. At positive voltages ( $V_G = 0, +10, +20, +40, +60$  V), the polarity has switched, but the integral is still close to zero. However, there exists a transition region ( $V_G = -20, -15, -10, -5$  V) in which the photocurrent is predominantly positive. This can also be seen in Fig. 2c, in which the integrated response exhibits a peak at  $V_G = -20$  V. The electrical characteristic, shown in the inset, depicts the typical shape observed in graphene devices, with a maximum resistance of  $R_g = 140\ \Omega$  at gate bias  $V_G = V_D$  ('Dirac voltage') of  $-5$  V. The maximum resistance and photoresponse do not occur at the same gate bias<sup>6,7</sup>.

To clarify the origin of this behavior, we studied devices consisting of only one pair of fingers and a long ( $\sim 2\ \mu\text{m}$ ) channel. This allowed us to clearly separate the photocurrent contributions from both electrodes, and in Fig. 2d,e we plot their dependence on gate voltage. In the device in Fig. 2d, both electrodes consist of palladium. The photocurrents generated around these two electrodes have the same magnitude, but opposite polarity. The sum of the two contributions is always close to zero (the small deviation from zero arises from imperfections of the device), regardless of

the gate bias. The flipping of the photocurrent polarity occurs at a gate bias  $V_G$  of  $\sim 20$  V before the Dirac point voltage is reached<sup>7,27</sup>, due to the p-doping of the graphene introduced by the palladium contact<sup>27</sup>. A schematic of the band profile is shown in the inset. In the other device (Fig. 2e), the two electrodes are made from palladium and titanium, respectively. The doping under the two electrodes is different, and the two contributions flip their polarity at different gate voltages. Consequently, when choosing the appropriate gate voltage, the photocurrents near both electrodes can flow in the same direction, leading to an enhanced overall photocurrent. The schematic of the band profile at this condition is shown in the inset of Fig. 2e.

After the photocurrent generation mechanism was clarified using a He-Ne laser with a wavelength of 632.8 nm and a spatial resolution of around  $0.6\ \mu\text{m}$ , 1.55- $\mu\text{m}$  light from a telecommunications laser was focused to a large spot, illuminating the entire photodetector (shown in the inset of Fig. 3b) for more photocurrent measurements. The gate-bias-dependent response, plotted in Fig. 3a, resembles the curve derived from the photocurrent images (Fig. 2c), and we determine  $V_G = -15$  V to be the optimum operation voltage. We kept this value fixed in further measurements. The gate bias ( $V_G$ ) can be readily reduced by using thinner gate oxide. Moreover, there is little power consumption associated with this relatively large gate bias due to the negligible gate leakage. The red curve in Fig. 3b shows the power dependence of the d.c. photocurrent without applying a bias between the interdigitated fingers. The response is linear up to a total optical incident power ( $P_{\text{opt}}$ ) on the entire device of 10 mW, and a photocurrent of  $15\ \mu\text{A}$  is observed, corresponding to an

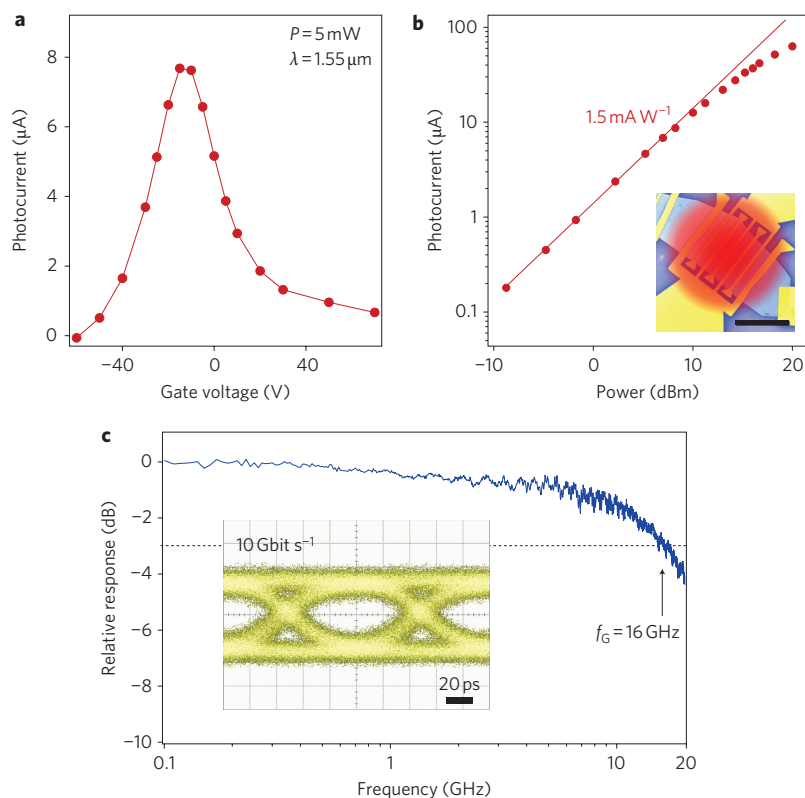


**Figure 3 | Photocurrent generation, high-frequency characterization of the MGM photodetector, and operation of the MGM photodetector at a data rate of 10 Gbit s<sup>-1</sup> with 1.55- $\mu$ m light excitation.** **a**, Photocurrent generated at zero source-drain bias versus back-gate bias. Spot size of the excitation light is  $\sim 5 \mu\text{m}$  in diameter. Total incident power is 5 mW. **b**, Total photocurrent generated at a back-gate bias of approximately  $-15 \text{ V}$  as a function of the incident power. Photocurrent saturation starts at an incident power of  $\sim 10 \text{ dBm}$ . The external responsivity before saturation is  $1.5 \text{ mA W}^{-1}$ . Inset: schematic of the illumination. Scale bar,  $5 \mu\text{m}$ . **c**, Relative photoresponse versus light intensity modulation frequency. The 3-dB bandwidth of this MGM photodetector is  $\sim 16 \text{ GHz}$ . Inset: receiver eye-diagram obtained using this MGM photodetector, showing a completely open eye. Scale bar, 20 ps.

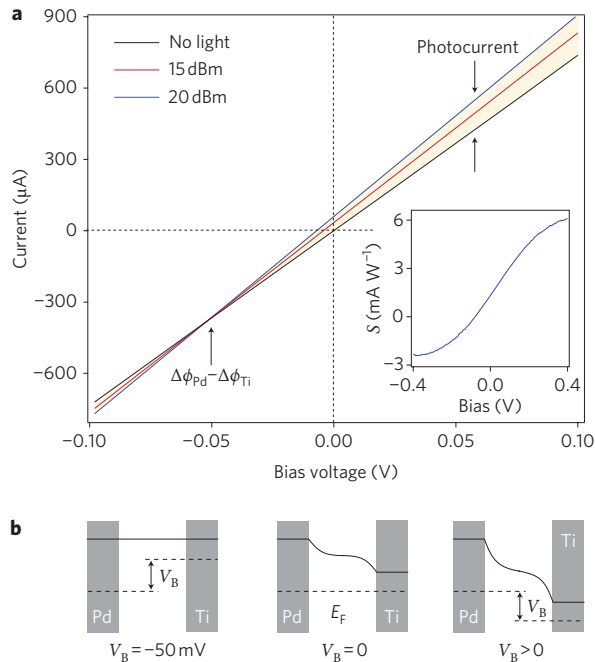
external responsivity of  $1.5 \text{ mA W}^{-1}$ . Further increase in the incident power leads to photocurrent saturation due to the screening effect as in conventional photodiodes<sup>28</sup>.

Figure 3c shows the relative a.c. photoresponse, measured using a commercial lightwave component analyser in combination with a network analyser. A modulated optical signal at a wavelength of 1,550 nm with an average power of 5 mW was focused onto the detector and the electrical output measured<sup>19</sup>. A 3-dB bandwidth of 16 GHz was determined. Owing to the exceptionally high carrier mobility and high saturation velocity, the bandwidth is not limited by the carrier transit time, but by the RC constant of the device. Compared with our previously measured graphene photodetector bandwidth, the bandwidth here is smaller. This is due to the relatively large area of the graphene used here, leading to a larger capacitance<sup>19</sup>.

To demonstrate the feasibility of using such graphene photodetectors in realistic optical applications, we used it in a  $10 \text{ Gbit s}^{-1}$  optical data link. The  $10 \text{ Gbit s}^{-1}$  electrical bit stream from a pseudo-random bit sequence (PRBS) generator with  $(2^{31}-1)$  pattern length was used to modulate light with a wavelength of 1,550 nm. The generated optical bit stream was then amplified to an output power of 17 dBm using an erbium-doped fibre amplifier (EDFA) and focused onto the graphene detector with zero source-drain bias. The output electrical data stream from the graphene detector was amplified and fed to an oscilloscope to obtain an 'eye diagram' (see Methods for details). As shown in the inset of Fig. 3c, a completely open eye at  $10 \text{ Gbit s}^{-1}$  was obtained, indicating that graphene can indeed be used for error-free optical data transmission.

The external responsivity (or efficiency) could be further improved by applying a bias within the photocurrent generation path. Figure 4a presents the drain-source bias ( $V_B$ ) dependence of the detector current (gate bias  $V_G$  stays fixed at  $-15 \text{ V}$ ). The black line shows the dark current ( $I_d$ ), which is simply given by Ohm's law:  $V_B/R_g$ , where  $R_g$  is the resistance of the graphene. Under optical illumination (red and blue curves in Fig. 4a), the total current  $I$  is the sum of the dark current and photocurrent:  $I = I_d + I_{ph}$ .  $I_{ph}$  increases for positive  $V_B$  (applied to the titanium electrode; palladium electrode grounded), but it decreases for  $0 > V_B > -50 \text{ mV}$  and changes sign at  $V_B < -50 \text{ mV}$ . All curves cross at  $V_B = -50 \text{ mV}$ ; that is, for this bias the photocurrent turns to zero regardless of the power of optical illumination. This behaviour clearly indicates that the  $E$ -field within the graphene channel can be influenced by applying a source-drain bias. Figure 4b shows schematically the band profiles for three different biases. The image in the middle presents the situation without bias between source and drain. In this case, as a result of the different doping introduced by titanium and palladium, a potential drop occurs within the graphene channel. The figure on the right shows the case for  $V_B > 0$ . Here, the external bias enhances the potential profile within the channel and the photocurrent increases. In contrast, at  $V_B = -50 \text{ mV}$  (left panel), the external bias just offsets the built-in potential profile, making the band profile flat and the photocurrent zero. We therefore estimate, for this graphene device, that the height of the potential within the channel induced by the doping of titanium and palladium is  $\sim 50 \text{ meV}$ .

The inset of Fig. 4a shows the bias dependence of the external responsivity  $S$ . As  $V_B$  increases,  $S$  rises monotonously and saturates



**Figure 4 | Source-drain bias ( $V_B$ ) dependence of the MGM photoresponse.**

**a**, Current versus source-drain bias ( $V_B$ ) with and without light illumination, at an excitation wavelength of  $1.55 \mu\text{m}$ . The difference between the coloured (blue and red) and black lines represents the photocurrent. Inset: measured external photoresponsivity of the MGM photodetector as a function of the source-drain bias. The coloured region denotes the magnitude of the photocurrent at an incident power of 20 dBm. **b**, The graphene band profiles (black lines) at source-drain biases ( $V_B$ ) of  $-50 \text{ mV}$ ,  $0$ , and positive bias, from left to right, respectively. Source-drain bias ( $V_B$ ) equals the difference in Fermi level between the palladium- and titanium-doped graphenes. The dotted line represents the Fermi level.

at  $V_B \approx 0.4 \text{ V}$ . A maximum responsivity of  $S = 6.1 \text{ mA W}^{-1}$  is achieved, which represents a 15-fold improvement over our previous graphene photodetector demonstration<sup>19</sup>. The dark current associated with the bias can possibly be suppressed through the creation of a significant electrical (transport) bandgap in biased bi-layer graphene<sup>29</sup>.

As well as the internal  $E$ -field due to band bending, which separates the photo-excited electron-hole pairs, photo-thermoelectric effects (PTE) can also contribute to photocurrent generation<sup>30</sup>. However, in our MGM photodetectors, we attribute the photocurrent generation primarily to the internal  $E$ -field because of the high photoresponsivity (or efficiency) and large operational bandwidth of the photodetector. The photoresponsivity of our MGM photodetector can be as high as  $6.1 \text{ mA W}^{-1}$  at room temperature, much larger than the previously reported photoresponsivity due to the PTE at single/bi-layer graphene interfaces. Moreover, the high bandwidth of the photoresponse also implies that the PTE is unlikely to be the dominant photocurrent-generation mechanism in the devices reported here.

In summary, we have used a graphene photodetector in a  $10 \text{ Gbit s}^{-1}$  optical data link at a wavelength of  $1.55 \mu\text{m}$ , and error-free detection has been achieved. Although the high-frequency photocurrent response experiments described here were performed at a single wavelength ( $1.55 \mu\text{m}$ ), we have also observed a strong photoresponse at the additional wavelengths of  $0.514 \mu\text{m}$  (ref. 8),  $0.633 \mu\text{m}$  (ref. 7) and  $2.4 \mu\text{m}$ . The photoresponse measurements at  $2.4 \mu\text{m}$  were performed using a pulsed optical parametric oscillator (OPO) source. The unique band structure of graphene can enable an ultrawide range of operational wavelengths,

at least from  $300 \text{ nm}$  to  $6 \mu\text{m}$ . In combination with its intrinsically high operating speed, this enables the graphene photodetector to be a promising candidate for a variety of applications including communications, remote sensing, environmental monitoring and surveillance<sup>20–23</sup>.

## Methods

All the measurements were performed in air at room temperature. To study the spatially resolved photoresponse we use a set-up consisting of a He-Ne laser (wavelength,  $632.8 \text{ nm}$ ) focused to a diffraction-limited spot ( $\sim 0.6 \mu\text{m}$ , full-width at half-maximum (FWHM) diameter) on the device using a  $\times 50$  microscope objective. A piezo-electrically driven mirror, mounted before the objective, allowed the beam to be positioned on the sample with high spatial precision. The laser beam was modulated with a mechanical chopper ( $\sim 1 \text{ kHz}$ ), and the short-circuit photocurrent signal was detected with a current pre-amplifier and a lock-in amplifier. The output of the lock-in was fed into a computer to construct the photocurrent image. The back-gate bias  $V_G$  was applied using an HP 4145C semiconductor parameter analyser.

A second set-up was used for high-speed optical characterization at a wavelength of  $1,550 \text{ nm}$ . In this arrangement, the light was focused with an IR lens to a large spot ( $\sim 5 \mu\text{m}$  FWHM diameter) to illuminate the entire active area of the MGM photodetector. Frequency response characterization was achieved using an Agilent Lightwave Component Analyzer N4375B. The optical fibre output of the LCA ( $0 \text{ dBm}$ ) was amplified using a PriTel erbium-doped fibre amplifier (EDFA), coupled into free space, and focused onto the device. The incident optical power on the sample was adjusted using neutral density filters. The photocurrent signal was extracted through a microwave probe from GGB Industries and fed into a parameter network analyser (Agilent E8364C). The frequency response (scattering parameter  $S_{21}$ ) was recorded as the modulation frequency was swept between  $10 \text{ MHz}$  and  $20 \text{ GHz}$ . This set-up allowed eye-diagram measurements to be carried out at a data rate of  $10 \text{ Gbit s}^{-1}$ . For this purpose, a Centellax TG1B1-A pseudo-random bit sequence generator was used to modulate the light from a  $1,550\text{-nm}$  laser with a JDS Uniphase Mach-Zehnder modulator. The optical signal was then amplified with the EDFA and focused onto the detector. A radio-frequency power amplifier with a gain of  $15 \text{ dB}$  and bandwidth of  $15 \text{ GHz}$  was used to amplify the detector output and the eye-diagram was measured with an Agilent 86100A wide-band oscilloscope. The gate bias was also applied using a HP 4145C semiconductor parameter analyser as mentioned above.

Received 1 November 2009; accepted 20 February 2010; published online 28 March 2010

## References

- Nakamura, S. & Fasol, G. *The Blue Laser Diode—GaN Based Light Emitters and Lasers* (Springer-Verlag, 1997).
- Soref, R. The past, present and future of silicon photonics. *IEEE J. Quantum Electron.* **12**, 1678–1687 (2007).
- Lipson, M. Guiding, modulating and emitting light on silicon—challenges and opportunities. *IEEE J. Lightwave Technol.* **23**, 4222–4238 (2005).
- Novoselov, K. S. *et al.* Electric field effect in atomically thin carbon films. *Science* **306**, 666–669 (2004).
- Zhang, Y., Tan, Y., Stromer, H. L. & Kim, P. Experimental observation of the quantum Hall effect and Berry's phase in graphene. *Nature* **438**, 201–204 (2005).
- Lee, E. J. H., Balasubramanian, K., Weitz, R. T., Burghard, M. & Kern, K. Contact and edge effects in graphene devices. *Nature Nanotech.* **3**, 486–490 (2008).
- Xia, F. *et al.* Photocurrent imaging and efficient photon detection in a graphene transistor. *Nano Lett.* **9**, 1039–1044 (2009).
- Mueller, T., Xia, F., Freitag, M., Tsang, J. & Avouris, Ph. Role of contacts in graphene transistors: a scanning photocurrent study. *Phys. Rev. B* **79**, 245430 (2009).
- Park, J., Ahn, Y. H. & Ruiz-Vargas, C. Imaging of photocurrent generation and collection in single-layer graphene. *Nano Lett.* **9**, 1742–1746 (2009).
- Nair, R. R. *et al.* Fine structure constant defines visual transparency of graphene. *Science* **320**, 1308 (2008).
- Mak, K. F., Sfeir, M. Y., Misewich, J. A. & Heinz, T. F. The electronic structure of few-layer graphene: probing the evolution from a two-dimensional to a three-dimensional material. Preprint at <<http://arXiv.org/abs/0908.0154v1>> (2009).
- Lin, Y. *et al.* 100 GHz transistors from wafer-scale epitaxial graphene. *Science* **327**, 662 (2010).
- Geim, A. K. Graphene: status and prospects. *Science* **324**, 1530–1534 (2009).
- Mak, K. F. *et al.* Measurement of the optical conductivity of graphene. *Phys. Rev. Lett.* **101**, 196405 (2008).
- Li, Z. Q. *et al.* Dirac charge dynamics in graphene by infrared spectroscopy. *Nature Phys.* **4**, 532–535 (2008).
- Wang, F. *et al.* Gate-variable optical transitions in graphene. *Science* **320**, 206–209 (2008).
- Zhang, Y. *et al.* Direct observation of a widely tunable bandgap in bilayer graphene. *Nature* **459**, 820–823 (2009).

18. Ryzhii, V., Mitin, V., Ryzhii, M., Ryabova, N. & Otsuji, T. Device model for graphene nanoribbon phototransistor. *Appl. Phys. Express* **1**, 063002 (2008).
19. Xia, F., Mueller, T., Lin, Y., Valdes-Garcia, A. & Avouris, Ph. Ultrafast graphene photodetector. *Nature Nanotech.* **4**, 839–843 (2009).
20. Rogalski, A., Antoszewski, J. & Faraone, L. Third-generation infrared photodetector arrays. *J. Appl. Phys.* **105**, 091101 (2009).
21. Kim, S. *et al.* Near-infrared fluorescent type II quantum dots for sentinel lymph node mapping. *Nature Biotechnol.* **22**, 93–97 (2003).
22. Xia, F. *et al.* An asymmetric twin-waveguide high-bandwidth photodiode using a lateral taper coupler. *IEEE Photon. Technol. Lett.* **13**, 845–847 (2001).
23. Tonouchi, M. Cutting-edge terahertz technology. *Nature Photon.* **1**, 97–105 (2007).
24. Liu, M. Y., Chen, E. & Chou, S. Y. 140-GHz metal–semiconductor–metal photodetectors on silicon-on-insulator substrate with a scaled active layer. *Appl. Phys. Lett.* **65**, 887–888 (1994).
25. Blake, P. *et al.* Making graphene visible. *Appl. Phys. Lett.* **91**, 063124 (2007).
26. Gaskell, P. E., Skulason, H. S., Rodenchuk, C. & Szkopek, T. Counting graphene layers on glass via optical reflection microscopy. *Appl. Phys. Lett.* **94**, 143101 (2009).
27. Giovannetti, G. *et al.* Doping graphene with metal contacts. *Phys. Rev. Lett.* **101**, 026803 (2008).
28. Li, N. *et al.* High-saturation-current charge-compensated InGaAs–InP uni-traveling-carrier photodiode. *IEEE Photon. Technol. Lett.* **16**, 864–866 (2004).
29. Xia, F., Farmer, D. B., Lin, Y.-M. & Avouris, Ph. Graphene field-effect transistors with high on/off current ratio and large transport band gap at room temperature. *Nano Lett.* **10**, 715–718 (2010).
30. Xu, X., Gabor, N. M., Alden, J. S., van der Zande, A. M. & McEuen, P. L. Photo-thermoelectric effect at a graphene interface. *Nano Lett.* **10**, 562–566 (2010).

### Acknowledgements

The authors would like to thank D.B. Farmer, B.A. Ek and J.J. Bucchignano for technical assistance. We are grateful to Y.A. Vlasov, W.M.J. Green and S. Assefa for lending us part of their equipment. T.M. acknowledges financial support by the Austrian Science Fund FWF (Erwin Schrödinger fellowship J2705-N16).

### Author contributions

All authors contributed to the preparation of this manuscript.

### Additional information

The authors declare no competing financial interests. Supplementary information accompanies this paper at [www.nature.com/naturephotonics](http://www.nature.com/naturephotonics). Reprints and permission information is available online at <http://npg.nature.com/reprintsandpermissions/>. Correspondence and requests for materials should be addressed to F.X. and P.A.